A Riemann Solver for Wet/Dry Interfaces in Geoclaw

Synthesis Paper

Name: Brian KYANJO

Committee: Dr. Jodi Mead, Michal Kopera, and Dylan Mikesell

Supervisor: Prof. Donna Calhoun

Date: October 6, 2021

1 Introduction

2 Riemann solvers

Riemann solvers are the numerical method in which time-averaged fluxes of all conserved quantities are calculated to solve fundamental problems in conservation laws named Riemann problems. A Riemann problem can be defined as a specific initial value problem (Cauchy) of a partial differential equation (PDE) that consists of conservation equations (1) combined with piece-wise constant initial data which has a single discontinuity in the domain of interest as shown in equation (2) [11].

$$q_t + f(q)_x = 0 \tag{1}$$

$$q(x,0) = \begin{cases} q_L, & \text{if } x \leq 0, \\ q_R, & \text{if } x > 0, \end{cases} \tag{2}$$

where $f(q)_x \in \mathbb{R}^m$ is a vector of conserved quantities, q_R and q_L are two piece-wise constant states separated by a discontinuity.

3 Shallow Water Equations (SWE)

The SWE are a system of hyperbolic PDEs governing the flow below a pressure surface in a fluid. They arise from the Navier-Stokes equations. In one dimension, the SWE can be used to model a fluid in a channel of unit width, taking the vertical velocity negligible, and horizontal velocity roughly constant throughout any cross section of the channel [13].

Consider small-amplitude waves in a one-dimensional fluid channel that is shallow relative to its wavelength. The conservation of momentum equation is written in terms of pressure, $p(x,t) = \frac{1}{2}\rho g h^2$, and the height field $h(x,t)$ (m), which breaks down into system (3).

$$h_t + (uh)_x = 0$$
$$(hu)_t + \left(hu^2 + \frac{1}{2}\rho g h^2\right)_x = 0 \tag{3}$$

where hu measures the flow rate of water past a point, ρ (kg/m^3) is the constant density of the incompressible fluid, and $u(x,t)$ (m/s) is the horizontal velocity. We will set $\rho = 1$ here.

A very simple set of initial conditions is a single discontinuity at the middle of the channel. In this case, we set h and hu equal to constants on either side of the channel. This problem is a classic Riemann Problem, and for the SWE, has an exact solution. We assume the discontinuity is at $x = 0$. The variation of h and hu on either side of the discontinuity leads the waves in the Riemann problem to move at different speeds creating discontinuities (shocks) or changing regions (rarefactions) [16]. At $x = 0$ and $t = 0$, the discontinuity is located between the left and right state, so the solution at the left (q_l) and right (q_r) states are given by:

$$q_l = \begin{bmatrix} h_l \\ (hu)_l \end{bmatrix} \quad \text{and} \quad q_r = \begin{bmatrix} h_r \\ (hu)_r \end{bmatrix} \tag{4}$$

As t increases, four distinct regions are created, separated by characteristics. The middle state called the intermediate state(q_m), is generated. The determination of this state characterizes the Riemann problem and how it connects to other states via waves in each respective characteristic family [1]. This can only hold if the connection wave speeds satisfy the Lax entropy condition. Figure 1 shows a wave combination of a centered rarefaction and shock wave from the first and second characteristic family respectively.
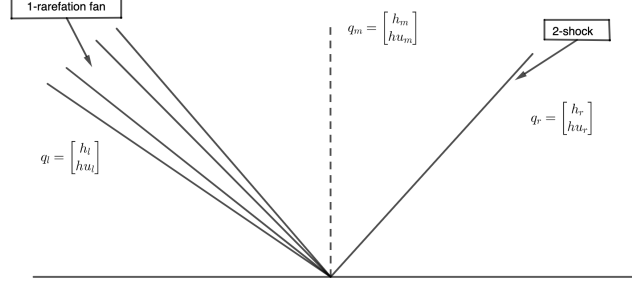

Figure 1: x-t plane showing the connection of states, 1-rarefaction fan, and the 2-shock.

The intermediate state is obtained by solving the Riemann problem using the exact or approximate method. Approximate methods are widely used due to their cheap computational cost compared to the exact solvers.

3.1 Exact Riemann Solver for two-shock SWE

The states in 1 are separated by either *shocks* or *rarefactions*. General left and right states will be connected by a combination of the two (either two shocks, two rarefactions, or one of each). We describe how to determine if two states are connected by a shock. We refer the reader to [16] for other cases.

We can obtain an exact solution to the Riemann Problem for the SWE as follows. The shock speed, $s(t)$, from the shock wave as the solution emerges is determined from the Rankine-Hugoniot jump condition given by equation (5) which must be satisfied across any shock wave. If q_l and q_r are connected by a shock, the Rankine Hugoniot conditions will be satisfied [20].

$$
\begin{aligned}
s_1(q_m - q_l) &= f(q_m) - f(q_l) \\
s_2(q_r - q_m) &= f(q_r) - f(q_m)
\end{aligned}
\tag{5}
$$

By applying condition (5) to shallow water equations (3) creates a system of four equations (6) that must be satisfied simultaneously.

$$
\begin{aligned}
s_1(h_m - h_l) &= hu_m - hu_l \\
s_1(hu_m - hu_l) &= hu_m^2 - hu_l^2 + \frac{1}{2}g(h_m^2 - h_l^2) \\
s_2(h_r - h_m) &= hu_r - hu_m \\
s_1(hu_r - hu_m) &= hu_r^2 - hu_m^2 + \frac{1}{2}g(h_r^2 - h_m^2)
\end{aligned}
\tag{6}
$$

Since the (h_l, u_l) and (h_r, u_r) are fixed, we find all states: (h_m, u_m) and their corresponding speeds: s_1 and s_2 that satisfy system (6). We have four equations and four unknowns, which gives a two parameter family of solutions: one-shock and two-shock. Using h_l and h_r as parameters, corresponding $u_l, u_r, s_1,$ and s_2 are determined for each h_l and h_r. And then a graph of hu against h is plotted that gives the curves in fig. 2. The point of intersection between the *1-shock (blue)* and *2-shock (orange)* physical solutions is the intermediate state q_m. The dotted curves represent unphysical solution [16].
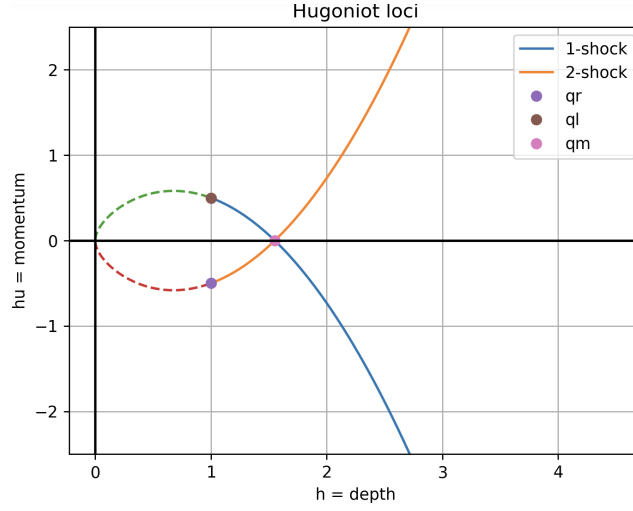
2

Figure 2: Shows curves that represent all states connected to q_l and all states connected to q_r via a *2-shock* and *1-shock* respectively. Equations (7) and (8) are solved to produce the curves.

Consider a general Riemann problem whose known solution consists of two shocks with initial data (4). This problem can be solved by finding the state q_m that can be connected to q_l by a *1-shock* and simultaneously connects to q_r by a *2-shock*. The point q_m lies on the curve (7) of points through point q_r that connects to q_r by a *2-shock* [3].

$$u_m = u_r + (h_m - h_r)\sqrt{\frac{g}{2}\left(\frac{1}{h_m} + \frac{1}{h_r}\right)} \tag{7}$$

Likewise, the state(q_m), must also lie on the Hugonoit locus (equation (8)) of the 1-shock wave passing through q_l

$$u_m = u_l - (h_m - h_l)\sqrt{\frac{g}{2}\left(\frac{1}{h_m} + \frac{1}{h_l}\right)} \tag{8}$$

Equations (7) and (8) form a system of two equations with two unknowns (h_m and u_m) that are equated since the left-hand sides of both equations are equal. A non linear equation that consist of only one unknown h_m is formed and solved using an iterative method such as Newton method to obtain a desired intermediate state in the Riemann solution [17].

As an example, consider a SWE Riemann problem with $h_l = h_r = 1, u_l = 0.5$, and $u_r = -0.5$. These initial values are used by the Newton solver to solve equations (7) and (8) to produce $h_m = 1.554$. The shock speeds (s_l and s_r) in each region are different due to different wave characteristics, we use this concept to loop through all interfaces and determine h and hu in each region as shown in the code 1 . At each interface the function *Riemann_solution*, is called and respective values of height (h) and momentum (hu) solutions are stored. According to Lax entropy conditions, a *1-shock* that physically connects q_l to q_m is obtained if $h_m > h_l$, and similarly a *2-shock* wave that physically connects q_m to q_r requires $h_m > h_r$ [17].

```
1   def Riemann_solution(ql,qr,qm,xi,g)      # xi = x/t
2   qm = array([hm,hum])    # intermediate state
3   sl = lambda h,ql: ql[1]/ql[0] - (1/ql[0] )*sqrt((g/2)*(ql[0]*h*(ql[0]+h)))
4   sr = lambda h,qr: qr[1]/qr[0] - (1/qr[0] )*sqrt((g/2)*(qr[0]*h*(qr[0]+h)))
5   if 0.5*(sl(hl,ql) + sl(hm,qm)) > xi : # left to middle state
6   h = hl
7   u = ul
8   hu = h*u
9   elif sl(hm,qm) < xi and xi < sr(hm,qr): # middle state
10  h = hm
11  u = um
12  hu = h*u
13  else:      # middle to right state
14  h = hr
```

3

```
15    u = ur
16    hu = h*u
17    return h, hu
18
```

Listing 1: Python code describing how the two shock case solution is obtained after the first time step.

The height field solution h obtained from the code 1 above is plotted in fig. 3. The plot depicts the left region being connected to the middle region via a *1-shock* wave and the middle being connected to the right region via a a *2-shock* wave.
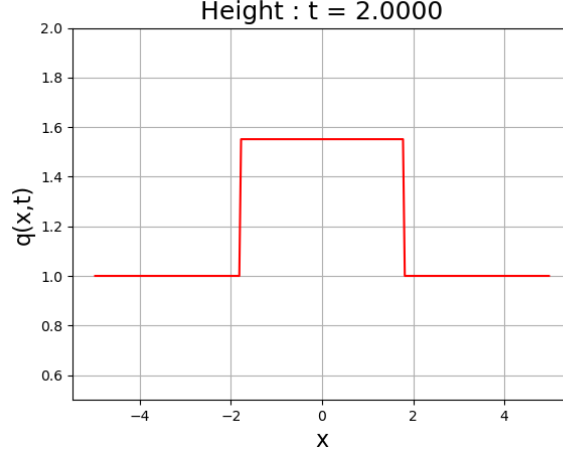

Figure 3: Shows all-shock Riemann exact solution

4   Finite volume discretization

Consider a one dimensional (1D) conservation law (equation (9)), where q is the measure of conserved quantity density and $f(q)$ is a flux function [11].

$$q_t(x,t) + f(q(x,t))_x = 0 \tag{9}$$

In finite volume methods (FVM), the domain is broken down into grid cells. Consider $C_i = (x_{i-\frac{1}{2}}, x_{i+\frac{1}{2}})$ to be the ith grid cell, the average value over the ith interval at time t^n is numerically approximated by Q_i^n in equation (10).

$$Q_i^n \approx \frac{1}{\Delta x} \int_{C_i} q(x, t^n) dx \tag{10}$$

where $\Delta t = (t^{n+1} - t^n)$ and $\Delta x = (x_{i+\frac{1}{2}} - x_{i-\frac{1}{2}})$ is the cell length. A discontinuity in q violates the PDE in the classical sense and only holds for the integral conservation law (fundamental equation (11)) [16]. Therefore at grid points near discontinuities where PDEs don't hold, all classical finite difference methods breakdown, resorting to FVM which are based on (11).

$$\frac{d}{dt} \int_{c_i} q(x, t) dx = f(q(x_{i-\frac{1}{2}}, t)) - f(q(x_{i+\frac{1}{2}}, t)) \tag{11}$$

The approximate total integral of q over each grid cell is evaluated and updated at every time step by the grid cell edge fluxes. The determined numerical flux functions evaluate the cell averages over a certain volume, which are used to approximate the solutions within the cells, using equation (12) [17].

$$Q_i^{n+1} = Q_i^n - \frac{\Delta t}{\Delta x}(F_{i+\frac{1}{2}}^n - F_{i-\frac{1}{2}}^n) \tag{12}$$

where $F_{i+\frac{1}{2}}^n$ is the average flux approximation along $x = x_{i-\frac{1}{2}}$. The Riemann problem is a fundamental tool in the evolution of FVM. Taking two neighbouring grid cells: $Q_{i-1} = q_L$ and $Q_i = q_R$ to be

cell averages, this information is used by the exact Riemann solver to compute numerical fluxes ($F^n_{i-\frac{1}{2}} = \mathcal{F}(Q_{i-1}, Q_i)$), that are used to update the cell average at each time step [1]. Then equation (12) becomes:

$$Q_i^{n+1} = Q_i^n - \frac{\Delta t}{\Delta x}\left[\mathcal{F}(Q_i, Q_{i+1}) - \mathcal{F}(Q_{i-1}, Q_i)\right] \tag{13}$$

where $\mathcal{F}$ is some numerical flux function.

5 Wave Propagation Algorithm (WPA)

Equation (12), can be reformulated as a first order wave propagation method by decomposing flux at the cell averages into fluctuations ($\mathcal{A}^+\Delta Q^n_{i-\frac{1}{2}}$ and $\mathcal{A}^-Q^n_{i+\frac{1}{2}}$) as shown in equations (14) and (15) [20].

$$\mathcal{A}^+\Delta Q^n_{i-\frac{1}{2}} = f(Q_i) - f(Q^*_{i-\frac{1}{2}}) \tag{14}$$

$$\mathcal{A}^-\Delta Q^n_{i+\frac{1}{2}} = f(Q^*_{i+\frac{1}{2}}) - f(Q_i) \tag{15}$$

where $\mathcal{A}^+\Delta Q^n_{i-\frac{1}{2}}$ and $\mathcal{A}^-Q^n_{i+\frac{1}{2}}$ are the net updating contributions from the rightward and leftward moving waves into the grid cell C_i from the right and left interface respectively, $Q^*_{i-\frac{1}{2}}$ is the intermediate cell average determined by the exact Riemann solver at $x_{i-\frac{1}{2}}$, and $f(Q^*_{i-\frac{1}{2}})$ is numerical flux at $Q^*_{i-\frac{1}{2}}$ [13]. Combining equations (14) and (15), the first order 1D wave propagation method is given by equation (16).

$$Q_i^{n+1} = Q_i^n - \frac{\Delta t}{\Delta x}(\mathcal{A}^+\Delta Q^n_{i-\frac{1}{2}} + \mathcal{A}^-Q^n_{i+\frac{1}{2}}) \tag{16}$$

The general conservation law in (9) can be written in *quasi-linear form* as

$$q_t + f'(q)q_x = 0 \tag{17}$$

where $f'(q) \in \mathbb{R}^{m \times m}$ flux Jacobian matrix. Consider a Riemann problem for the system (17) with initial data

$$q(x, t^n) = \begin{cases} Q^n_{i-1} & \text{if} \quad x < x_{i-\frac{1}{2}} \\ Q^n_i & \text{if} \quad x > x_{i-\frac{1}{2}} \end{cases} \tag{18}$$

The initial data (equation (18)), is used by the exact Riemann solver to generate an intermediate state ($q_m = (h_m, hu_m)^T$), which is used to evaluate the eigenvalues ($\lambda_{i-1/2}$) and eigenvectors ($r_{i-1/2}$) at $x = x_{i-\frac{1}{2}}$. The pth wave at interface $i-1/2$ is given by $\mathcal{W}^p_{i-1/2} \equiv \alpha_{i-\frac{1}{2}} r^p_{i-\frac{1}{2}}$ with speeds $s^p_{i-1/2} = \lambda^p_{i-1/2}$ [16]. where $\alpha_{i-\frac{1}{2}}$ depicts the coefficients of the the eigenvectors. Waves and speeds are obtained as an eigenvector decomposition of the jump in Q_i at the interface $i - \frac{1}{2}$. This decomposition takes the form

$$Q_i - Q_{i-1} = \sum_{p=1}^{m} \alpha_{i-\frac{1}{2}} r_{i-\frac{1}{2}} \tag{19}$$

The wave speed $s^p_{i-\frac{1}{2}}$ associated with the vector $r^p_{i-\frac{1}{2}}$, are preselected basing on the characteristic structure of the initial Riemann data [13]. Therefore the fluctuations $\mathcal{A}^+\Delta Q^n_{i-\frac{1}{2}}$ and $\mathcal{A}^-\Delta Q^n_{i-\frac{1}{2}}$ are defined by equations (20) and (21):

$$\mathcal{A}^- \Delta Q^n_{i-\frac{1}{2}} = \sum_{\{p:s^p_{i-\frac{1}{2}}<0\}} s^p_{i-\frac{1}{2}} \mathcal{W}^p_{i-\frac{1}{2}} \tag{20}$$

$$\mathcal{A}^+ \Delta Q^n_{i-\frac{1}{2}} = \sum_{\{p:s^p_{i-\frac{1}{2}}>0\}} s^p_{i-\frac{1}{2}} \mathcal{W}^p_{i-\frac{1}{2}} \tag{21}$$

In a standard conservative case ((9)), the sum of the left-going and right-going fluctuations should satisfy:

$$\mathcal{A}^+ \Delta Q^n_{i-\frac{1}{2}} + \mathcal{A}^- Q^n_{i+\frac{1}{2}} = f(Q_i) - f(Q_{i-1}) \tag{22}$$

The second order accuracy is obtained by taking the correction terms into account as shown described in equation (23) [2]

$$Q_i^{n+1} = Q_i^n - \frac{\Delta t}{\Delta x}(\mathcal{A}^+ \Delta Q^n_{i-\frac{1}{2}} + \mathcal{A}^- Q^n_{i+\frac{1}{2}}) - \frac{\Delta t}{\Delta x}(\tilde{F}^n_{i+\frac{1}{2}} - \tilde{F}^n_{i-\frac{1}{2}}) \tag{23}$$

where $\tilde{F}^n_{i-\frac{1}{2}}$ are second order correction terms determined by the waves and speeds in the Riemann problems after approximating the average flux along $x = x_{i-\frac{1}{2}}$:

$$\tilde{F}^n_{i-\frac{1}{2}} = \frac{1}{2}\sum_{p=1}^{m}|s^p_{i-\frac{1}{2}}|\left(1 - \frac{\Delta t}{\Delta x}|s^p_{i-\frac{1}{2}}|\right)\tilde{\mathcal{W}}^p_{i-\frac{1}{2}} \tag{24}$$

Here $\tilde{\mathcal{W}}^p_{i-\frac{1}{2}}$ depicts a limited version of the wave $\mathcal{W}^p_{i-\frac{1}{2}}$, which is obtained after a comparison between $\mathcal{W}^p_{i-\frac{1}{2}}$ and $\mathcal{W}^p_{i-\frac{3}{2}}$ when $s^p > 0$ [1].

5.1 WPA for the Shallow Water Equations

The combination of equations in system (3), forms a system of one-dimensional SWEs given by equation (25)

$$\begin{bmatrix} h \\ hu \end{bmatrix}_t + \begin{bmatrix} uh \\ hu^2 + \frac{1}{2}gh^2 \end{bmatrix}_x = 0 \tag{25}$$

Equation (25) can be written as a quasi-linear system as shown in equation (26):

$$\begin{bmatrix} h \\ hu \end{bmatrix}_t + \begin{bmatrix} 0 & 1 \\ -u^2 + gh & 2u \end{bmatrix}\begin{bmatrix} h \\ hu \end{bmatrix}_x = \begin{bmatrix} 0 \\ 0 \end{bmatrix} \tag{26}$$

where the flux Jacobian matrix $f'(q)$ is given by

$$f'(q) = \begin{bmatrix} 0 & 1 \\ -u^2 + gh & 2u \end{bmatrix} \tag{27}$$

The non linear problem (equation (9)), can be replaced by a linearized problem defined locally at each cell interface [17],

$$\hat{q}_t + \hat{A}_{i-\frac{1}{2}}\hat{q}_x = 0 \tag{28}$$

where 2×2 matrix $\hat{A}_{i-\frac{1}{2}}$ (equation (29)) is selected to be an approximation of $f'(q)$ that is valid in the neighbourhood of the intial data Q_{i-1} and Q_i.

$$\hat{A}_{i-\frac{1}{2}} = \begin{bmatrix} 0 & 1 \\ -\hat{u}^2 + g\bar{h} & 2\hat{u} \end{bmatrix} \tag{29}$$

where $\bar{h} = \frac{1}{2}(h_{i-1} + h_i)$ is the average between end points h_{i-1} and h_i, g is the acceleration due to gravity, and $\hat{u} = (\sqrt{h_{i-1}}u_{i-1} + \sqrt{h_i}u_i)/(\sqrt{h_{i-1}} + \sqrt{h_i})$ is the Roe average. Since $\hat{A}_{i-\frac{1}{2}}$ is a real diagonalizable Jacobian matrix evaluated at $\hat{q} = (\bar{h}, \bar{h}\hat{u})$, then its eigenvalues $(\hat{\lambda})$ and eigenvectors $(\hat{r})$ are given by equations (30) and (31) respectively [18].

$$\hat{\lambda}^1 = \hat{u} - \hat{c}, \qquad \hat{\lambda}^2 = \hat{u} + \hat{c} \tag{30}$$

$$\hat{r}^1 = \begin{bmatrix} 1 \\ \hat{\lambda}^1 \end{bmatrix}, \qquad \hat{r}^2 = \begin{bmatrix} 1 \\ \hat{\lambda}^2 \end{bmatrix} \tag{31}$$

where $\hat{c} = \sqrt{gh}$, the approximate Riemann solver is used to decompose the vector $\delta \equiv Q_i - Q_{i-1}$ into two waves: $\alpha^1_{i-\frac{1}{2}}\hat{r}^1$ and $\alpha^1_{i-\frac{1}{2}}\hat{r}^2$ as

$$Q_i - Q_{i-1} = \alpha^1_{i-\frac{1}{2}}\hat{r}^1 + \alpha^1_{i-\frac{1}{2}}\hat{r}^2 \equiv \mathcal{W}^1_{i-\frac{1}{2}} + \mathcal{W}^2_{i-\frac{1}{2}} \tag{32}$$

where the coefficients $\alpha^1_{i-\frac{1}{2}}$ are given by:

$$\alpha^1_{i-\frac{1}{2}} = \frac{(\hat{u} + \hat{c})\delta^1 - \delta^2}{2\hat{c}} \tag{33}$$

$$\alpha^2_{i-\frac{1}{2}} = \frac{-(\hat{u} - \hat{c})\delta^1 + \delta^2}{2\hat{c}} \tag{34}$$

6 Numerical Examples

Figures 4a and 4b, represents two plots: first and second order correction (without limiters) obtained from simulation of WPA flux formulation [1]and WPA using the Roe solver [2] combined with the exact Riemann solver [13]. The dam break problem is solved using both flux formulation and Roe solver, and solutions are validated against the exact Riemann solver solution as shown in the two figures. For the first order solution both methods coincide even though they tend to flatten at both edges of the 1-rarefaction fan and the 2-shock. On applying the second order correction in 4b, the solutions at edges of each region tend to converge more to the exact solution, however more noise is exhibited at the beginning and end of the intermediate region, and this can be solved by applying limiters to the approximate solutions as shown in fig. 5.

Accuracy of smooth solutions are obtained by advancing first order methods to second order accurate, but these still fail at the neighbourhood of discontinuities, where oscillations (noise) are created as shown in fig. 4b. Limiters use the characteristics of the solution at such regions to filter out the oscillations eliminating the phase error hence increasing accuracy as depicted in fig. 5. This figure depicts the filtration of oscillations around the 1-rarefaction fan and 2-shock discontinuity regions in fig. 4b after application of limiters at the final time. It's seen that the height field solution exhibits a smooth through out the the entire simulation even at jumps in the solution compared to fig. 4b. This improved the accuracy of the second order method, simulating well the boundaries of several regions without noise.

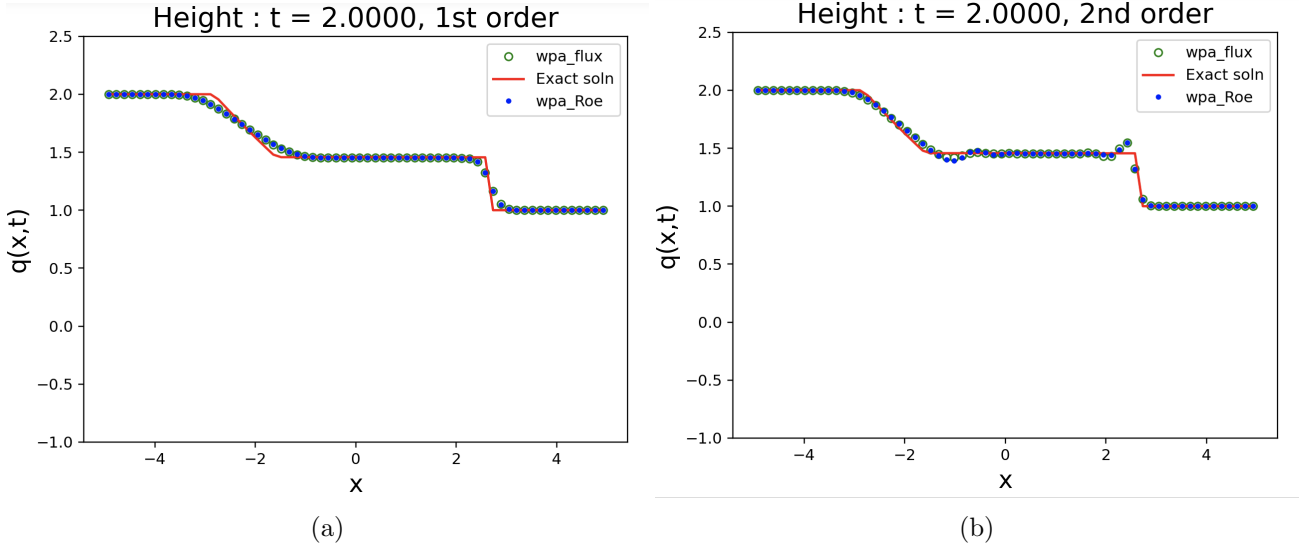(a)   (b)

Figure 4: (a) and (b) respectively show height field at the final time step for both first and second order correction without limiters using 64 space points.
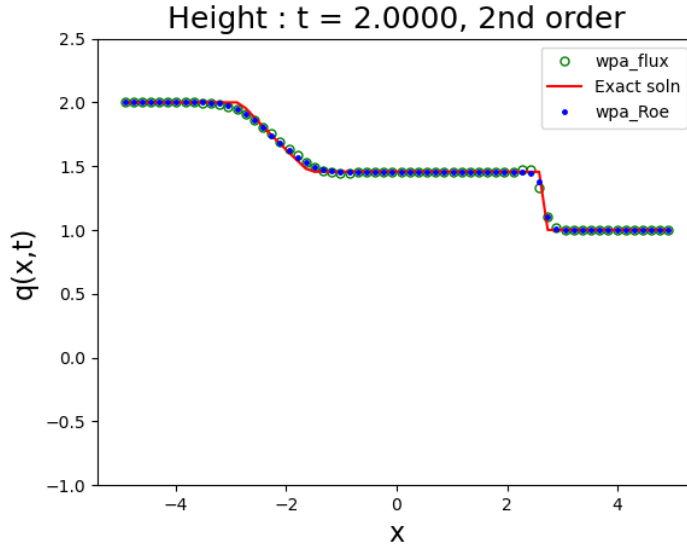

Figure 5: Shows the height field at the final time step of second order correction with limiter using 64 space points.

6.1 Bathymetric source terms

Equation (3), can be extended to balance equations by introducing a bathymetric source term as shown in equation (35). This is done by discretising the source term to generate values $-gh_{i-\frac{1}{2}}B'(x_{i-\frac{1}{2}})$ at cell interfaces $x = x_{i-\frac{1}{2}}$. This approach is very useful, because the discrepancy caused due to the failure of the flux gradient to counterbalance the source term in a near steady state solution is decomposed into propagating waves making the approach more robust than the quasi-steady WPA [1].

$$h_t + (uh)_x = 0$$
$$(hu)_t + \left(hu^2 + \frac{1}{2}gh^2\right)_x = -ghB'(x) \tag{35}$$

where $B(x)$ represents bottom elevation.

The fwaves are introduced to handle the stationery states and also solve accurately the quasi-steady problems in which the objective is to obtain propagation due to small amplitude perturbations. The standard WPA (5) is conservative if and only if equation (36) is satisfied, but the flux-based wave decomposition yields a more flexible algorithm that is conservative even when equation(36) is not satisfied. And works perfect even for problems in which the Roe average is not easily computed [1].

$$A_{i-\frac{1}{2}}(Q_i - Q_{i-1}) = f(Q_i) - f(Q_{i-1}) \tag{36}$$

The flux difference $f(Q_i) - f(Q_{i-1})$ is directly decomposed as a linear combination of the eigenvectors $r_{i-\frac{1}{2}}$ as shown in equation (37) [2]

$$f(Q_i) - f(Q_{i-1}) - \Delta x \psi_{i-\frac{1}{2}} = \sum_{p=1}^{m} \beta_{i-\frac{1}{2}}^{p} r_{i-\frac{1}{2}}^{p} \equiv \sum_{p=1}^{m} \mathcal{Z}_{i-\frac{1}{2}}^{p} \tag{37}$$

where

$$\beta_{i-\frac{1}{2}} = R_{i-\frac{1}{2}}^{-1}(f(Q_i) - f(Q_{i-1})) - \Delta x \psi_{i-\frac{1}{2}} \tag{38}$$

The vectors $\mathcal{Z}^p = \beta^p r^p$ are called the fwaves, as they are similar to the waves $\mathcal{W}^p$ though they carry flux increments rather than q increments. The standard WPA (5) first and second order corrections have been advanced to capture the flux based wave decomposition by changing equations (19) and (24) to (38) and (39) respectively.

$$\tilde{F}_{i-\frac{1}{2}}^{n} = \frac{1}{2} \sum_{p=1}^{m} \text{sgn}(s_{i-\frac{1}{2}}^{p}) \left(1 - \frac{\Delta t}{\Delta x}|s_{i-\frac{1}{2}}^{p}|\right) \tilde{\mathcal{Z}}_{i-\frac{1}{2}}^{p} \tag{39}$$

where $\tilde{\mathcal{Z}}_{i-\frac{1}{2}}^{p}$ is also a limited version of the f-wave $\mathcal{Z}_{i-\frac{1}{2}}^{p}$, obtained in the same way as $\tilde{\mathcal{W}}_{i-\frac{1}{2}}^{p}$ was obtained from $\mathcal{W}_{i-\frac{1}{2}}^{p}$ 17. As seen in fig. 6b, the second order correction term for the f-wave approach(wpa_flux) phased out the oscillations near discontinuities without employing any limiter compared to the Roe-solver that employed the standard WPA. This means that the stationery waves near the discontinuities have been handled by the f-wave approach.

Figures. 6a and 6b, depicts the first and second order correction of the flux base wave decomposition(green)[1], exact Riemann solution(red), and Roe-solver(blue) based on the standard WPA for the dam break problem height field simulated at the final time without limiters. Fig. 6a shows that both solutions coincide, but the difference is exhibited in the 6b in which the Roe solver is highly affected by the oscillations near discontinuities in absence of limiters. This basically means that the f-wave approach together with the flux term filtered out the oscillatory terms.

(a)   (b)
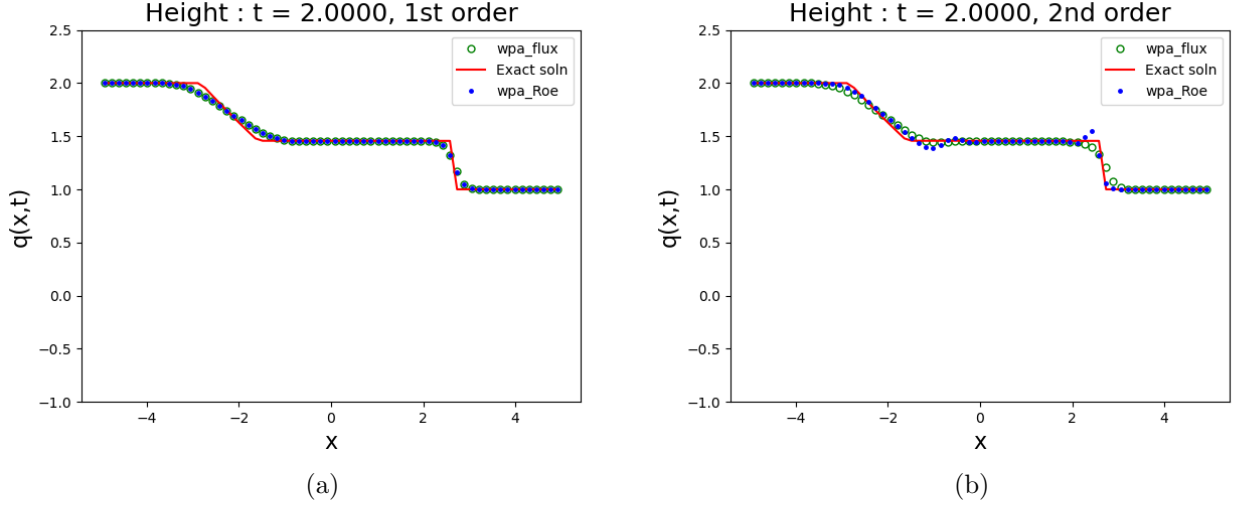
Figure 6: (a) and (b) respectively show height field at the final time step for both first and second order correction without limiters obtained after introducing the source term and the f-wave method.

Figure. 7 represents Figure. 6b with limiters used. The limiters made the Roe solver solution non oscillatory(smooth through out), and rectified the solution of the f-wave approach to replicate the jump at the 2-shock but no stationary wave was present in the solution.
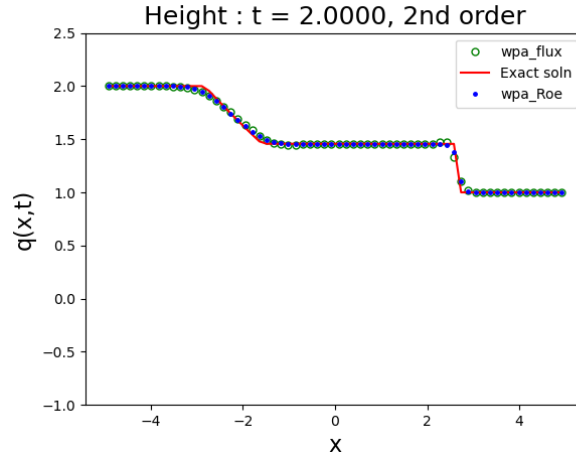

Figure 7: Shows the height field at the final time step of second order correction with limiter obtained after introducing the source term and the f-wave method using 64 space points.

7   Riemann Problem for Wet/Dry States

In the previous section we discussed how the exact solver solved the Riemann problem for cases in which the water height field is strictly positive everywhere. According to (author?) [24], dry states are regions with zero water depth. In such states SWEs are not applicable, so we consider wet states adjacent to dry regions as shown in figure 8. This enables solving SWEs in wet states, right up the boundary between wet and dry states [17].
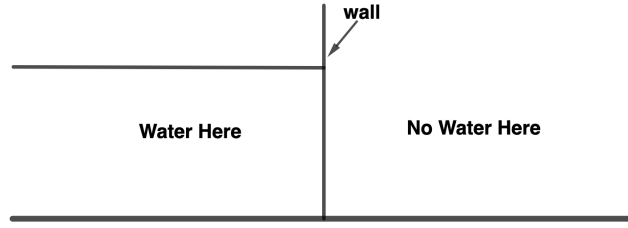
Figure 8: The Riemann problem with a dry bed (has no water) in one of the data state.

In both (author?) [2] and (author?) [24], there are three possible cases of wet/dry interfaces to consider as illustrated in fig. 9. Case (a) right dry bed, the solution exhibits *1-rarefaction* wave associated with the left eigenvalue $\lambda_1 = u - a$. Case (b) Left dry bed, the solution exhibits *2-rarefaction* wave associated with the right eigenvalue $\lambda_2 = u + a$. Case (c) dry bed doesn't exit at $t = 0$, but is created in the interaction between the two left and right wet bed regions if $S_{*L} \leq S_{*R}$ where $a = \sqrt{gh}$ [17].
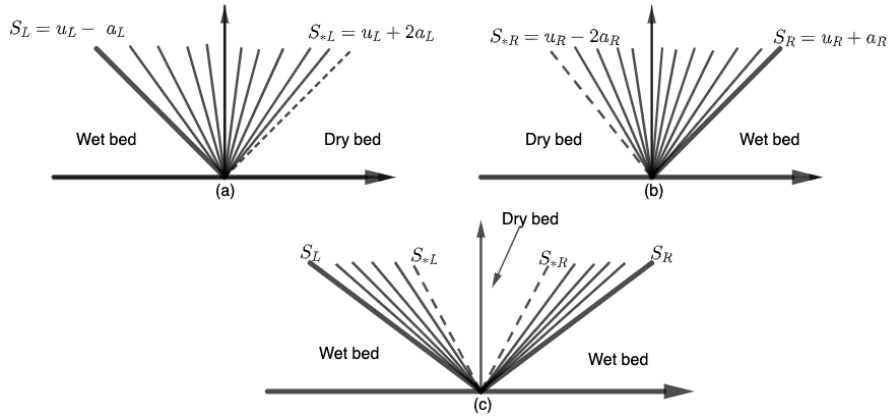

Figure 9: The dry state appears in three cases: (a) dry region is on the right, (b) dry region is on the left, and (c) dry region appears in the interaction of two wet bed states.

Figure 10a and 10b respectively show solution profiles for the height field for cases (a) and (b) at the final time step for a Riemann problem solved exactly with initial data containing dry bed regions appearing on the right and left.
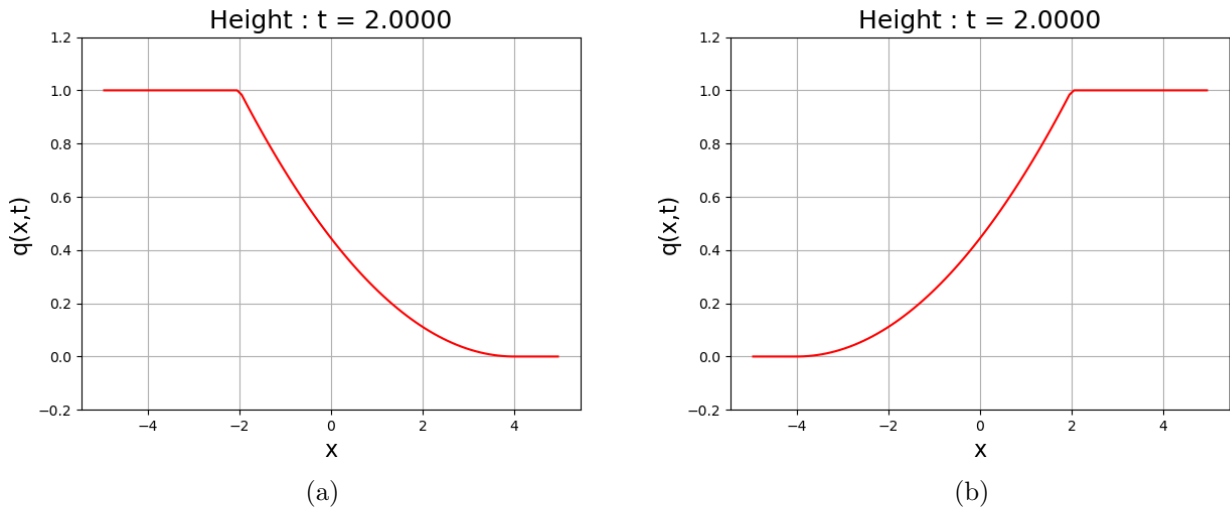

Figure 10: (a) and (b) respectively Shows a typical solution profile for the Riemann solution in which the dry bed is at the right and left.

Figure 11 show solution profiles for the height field for case (c) at the final time step for a Riemann problem solved exactly for which a dry bed region appears due to the interaction of two wet bed states satisfying $S_{*L} \leq S_{*R}$.
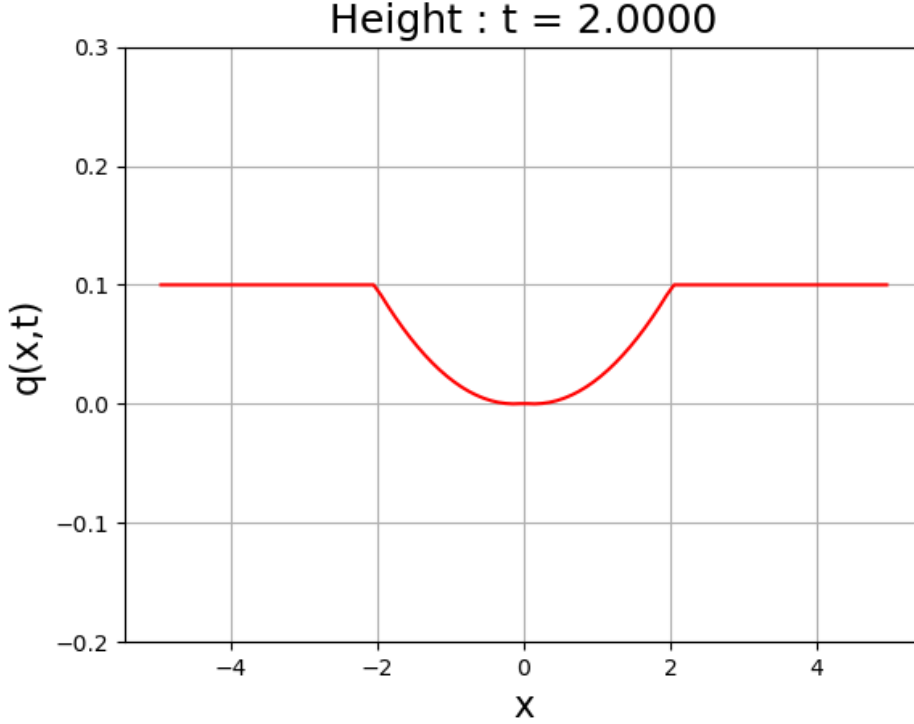

Figure 11: Shows a typical solution profile for the Riemann solution in which the dry bed appears in the interaction between the two wet bed regions.

Here, we describe the approach taken by (author?) [13]. (author?) [18] proposed that equation (25) can be decomposed into equation (40):

$$\begin{bmatrix} H_i - H_{i-1} \\ HU_i - HU_{i-1} \\ \varphi(Q_i) - \varphi(Q_{i-1}) \end{bmatrix} = \sum_{p=1}^{3} \alpha_{i-\frac{1}{2}}^{p} w_{i-\frac{1}{2}}^{p} \tag{40}$$

where the momentum flux $\varphi(q) = (hu^2 + \frac{1}{2}gh^2)$, $Q_i = (H_i, HU_i)^T$ represents the numerical solution of $q = (h, hu)^T$ in C_i, and $w_{i-\frac{1}{2}}^{p} \in \mathbb{R}^3$, $\forall$ $p \in [1,3]$ with p a set of chosen independent vectors.

The decomposition of the solutions $Q_i - Q_{i-1}$ and $f(Q_i) - f(Q_{i-1}) \in \mathbb{R}^2$ are represented by the first two and last two components of the three components of the decomposition (40) respectively. Conservation is maintained by modifying fluctuations using the last two of the three components in equation (40) [1]. Then consider $z_{i-\frac{1}{2}}^{p} \in \mathbb{R}^2$ for each $p \in [1,3]$ to be flux waves defined by:

$$z_{i-\frac{1}{2}}^{p} = [\mathbf{0}_{2\times 1} \quad \mathbf{I}_{2\times 2}] \alpha_{i-\frac{1}{2}}^{p} w_{i-\frac{1}{2}}^{p} \tag{41}$$

where $\mathbf{0}_{2\times 1}$ is a two by one zeros matrix, $\mathbf{I}_{2\times 2}$ is a two by two identity. Then updated fluctuations become:

$$\mathcal{A}^{+}\Delta Q_{i-\frac{1}{2}}^{n} = \sum_{\{p:s_{i-\frac{1}{2}}^{p}>0\}} z_{i-\frac{1}{2}}^{p} \tag{42}$$

$$\mathcal{A}^{-}\Delta Q_{i+\frac{1}{2}}^{n} = \sum_{\{p:s_{i+\frac{1}{2}}^{p}<0\}} z_{i+\frac{1}{2}}^{p} \tag{43}$$

Equations 42 and 43 are determined by decomposing flux in a similar way as in the f-wave approach in (author?) [1] and (author?) [12], however in (author?) [13] its decomposed into three waves ($w_{i-\frac{1}{2}}^p \in \mathbb{R}^3$) with three associated wave speeds ($s_{i-\frac{1}{2}}^p$ for $p = 1, 2, 3$) rather than two allowing a more accurate approximation to the Riemann problem with a large rarefaction and a natural entropy fix for transonic rarefactions. The first and third eigen pairs $\{w_{i-\frac{1}{2}}^{1,3}, s_{i-\frac{1}{2}}^{1,3}\}$ are related to the eigen pairs of (27), even though in (author?) [3], its the first and second pairs that relate to the original fields of SWE.

Therefore from the three eigen pairs, we choose,

$$\{w_{i-\frac{1}{2}}^1, s_{i-\frac{1}{2}}^1\} = \{(1, \check{s}_{i-\frac{1}{2}}^-, (\check{s}_{i-\frac{1}{2}}^-)^2)^T, \check{s}_{i-\frac{1}{2}}^-\}$$
$$\{w_{i-\frac{1}{2}}^3, s_{i-\frac{1}{2}}^3\} = \{(1, \check{s}_{i-\frac{1}{2}}^+, (\check{s}_{i-\frac{1}{2}}^+)^2)^T, \check{s}_{i-\frac{1}{2}}^+\} \tag{44}$$

where $\check{s}_{i-\frac{1}{2}}^\pm$ are the Einfeldt speeds [2, 13, 3] defined by:

$$\check{s}_{i-\frac{1}{2}}^- = \min(\lambda^-(Q_{i-1}^n), \hat{\lambda}_{i-\frac{1}{2}}^-)$$
$$\check{s}_{i-\frac{1}{2}}^+ = \max(\lambda^+(Q_i^n), \hat{\lambda}_{i-\frac{1}{2}}^+) \tag{45}$$

where $\lambda^\pm = u \pm \sqrt{gh}$ are eigen values of equation (27) and $\check{\lambda}_{i-\frac{1}{2}}^\pm$ are eigen values of the Roe averaged Jacobian matrix $\hat{A}_{i-\frac{1}{2}}$ in equation (29). The second pair $\{w_{i-\frac{1}{2}}^2, s_{i-\frac{1}{2}}^2\}$ that result into the second wave named corrector wave and speed is arbitrary chosen in various ways. The corrector wave corrects inaccurate, non-conservative and entropy violating approximate Riemann solutions with only two waves [3].

There is only one rarefaction in the exact Riemann solution, that connects wet to dry state. The developing wet/dry interface is in this case single edge of the rarefaction, making it possible to determine the interface propagating speed using the corresponding characteristics field of the Riemann invariants [17]. In (author?) [12] and [13], Einfeldt speeds ((45)) define two propagating discontinuities, the middle state between them is determined to maintain conservation and its depth at interface $x_{i-\frac{1}{2}}$ is given by:

$$\check{H}_{i-\frac{1}{2}}^* = \frac{HU_{i-1} - HU_i + \check{s}_{i-\frac{1}{2}}^+ H_i - \check{s}_{i-\frac{1}{2}}^- H_{i-1}}{\check{s}_{i-\frac{1}{2}}^+ - \check{s}_{i-\frac{1}{2}}^-} \tag{46}$$

The wet/dry interface propagation speed is given by equation (47), since the right state in figure 8, is considered as the initial dry state, which also makes the rarefaction to be in the first characteristic field as shown in figure 9.(a) [13].

$$s_{i-\frac{1}{2}}^3 = \check{s}_{i-\frac{1}{2}}^+ = \lambda_{i-\frac{1}{2}}^{-*}(H_{i-\frac{1}{2}}^* = 0) = U_{i-1} - 2\sqrt{gH_{i-1}} \tag{47}$$

If the left state in figure 8, is considered as the initial dry state, then the wet/dry interface propagation speed is given by equation (48), and the rarefaction is in the second characteristic field as shown in figure 9.(b) [13].

$$s_{i-\frac{1}{2}}^1 = \check{s}_{i-\frac{1}{2}}^- = \lambda_{i-\frac{1}{2}}^{+*}(H_{i-\frac{1}{2}}^* = 0) = U_i - 2\sqrt{gH_i} \tag{48}$$

Note that the middle state depth $H_{i-\frac{1}{2}}^* = 0$ since it corresponds to the initial dry state

8 Future research directions

References

[1] Derek Bale, Randall J. LeVeque, Sorin Mitran, and James Rossmanith. A Wave Propagation Method for Conservation Laws and Balance Laws with Spatially Varying Flux Functions. 24(3):955–978, 2003.

[2] Mina Barzgaran, Hossein Mahdizadeh, and Soroosh Sharifi. Numerical simulation of bedload sediment transport with the ability to model wet/dry interfaces using an augmented riemann solver. *Journal of Hydroinformatics*, 21(5):834–850, 2019.

[3] Marsha J. Berger, David L. George, Randall J. LeVeque, and Kyle T. Mandli. The GeoClaw software for depth-averaged flows with adaptive refinement. 34(9):1195–1206, September 2011. arXiv:1008.0455v2 [physics.geo-ph].

[4] Sheng Bi, Jianzhong Zhou, Yi Liu, and Lixiang Song. A finite volume method for modeling shallow flows with wet-dry fronts on adaptive cartesian grids. *Mathematical problems in Engineering*, 2014, 2014.

[5] Onno Bokhove. Flooding and drying in discontinuous galerkin finite-element discretizations of shallow-water equations. part 1: one dimension. *Journal of scientific computing*, 22(1):47–82, 2005.

[6] Andreas Buttinger-Kreuzhuber, Zsolt Horváth, Sebastian Noelle, Günter Blöschl, and Jürgen Waser. A fast second-order shallow water scheme on two-dimensional structured grids over abrupt topography. *Advances in water resources*, 127:89–108, 2019.

[7] Elmiloud Chaabelasri, Mohamed Jeyar, Najim Salhi, and Imad Elmahi. A simple unstructured finite volume scheme for solving shallow water equations with wet/dry interface. *International Journal of Mechanical Engineering and Technology*, 10(1):2019, 1849.

[8] Frédéric Dias and Denys Dutykh. Dynamics of tsunami waves. In *Extreme man-made and natural hazards in dynamics of structures*, pages 201–224. Springer, 2007.

[9] Denys Dutykh and Frédéric Dias. Water waves generated by a moving bottom. In *Tsunami and Nonlinear waves*, pages 65–95. Springer, 2007.

[10] Martin Fišer, Ilhan Özgen, Reinhard Hinkelmann, and Jan Vimmr. A mass conservative well-balanced reconstruction at wet/dry interfaces for the godunov-type shallow water model. *International Journal for Numerical Methods in Fluids*, 82(12):893–908, 2016.

[11] D. L. George. Adaptive finite volume methods with well-balanced Riemann solvers for modeling floods in rugged terrain: Application to the Malpasset dam-break flood (France, 1959). 66(8):1000–1018, 2011.

[12] David L George. *Finite volume methods and adaptive refinement for tsunami propagation and inundation.* University of Washington, 2006.

[13] David L. George. Augmented Riemann solvers for the shallow water equations over variable topography with steady states and inundation. 227(6):3089 – 3113, 2008.

[14] Yuxin Huang, Ningchuan Zhang, and Yuguo Pei. Well-balanced finite volume scheme for shallow water flooding and drying over arbitrary topography. *Engineering Applications of Computational Fluid Mechanics*, 7(1):40–54, 2013.

[15] Ethan J Kubatko, Joannes J Westerink, and Clint Dawson. Semi discrete discontinuous galerkin methods and stage-exceeding-order, strong-stability-preserving runge–kutta time discretizations. *Journal of Computational Physics*, 222(2):832–848, 2007.

[16] Randall J LeVeque et al. *Finite volume methods for hyperbolic problems*, volume 31. Cambridge university press, 2002.

[17] Randall J. LeVeque, David L. George, and Marsha J. Berger. Tsunami modelling with adaptively refined finite volume methods. 20:211 – 289, May 2011.

[18] Randall J LeVeque and Marica Pelanti. A class of approximate riemann solvers and their relation to relaxation schemes. *Journal of Computational Physics*, 172(2):572–591, 2001.

[19] Dingzhu Liu, Jinbo Tang, Hao Wang, Yang Cao, Nazir Ahmed Bazai, Huayong Chen, and Daochuan Liu. A new method for wet-dry front treatment in outburst flood simulation. *Water*, 13(2):221, 2021.

[20] Kyle T. Mandli, Aron. J. Ahmadia, Marsha Berger, Donna Calhoun, David L. George, Yannis Hadjimichael, David I. Ketcheson, Grady I. Lemoine, and Randall J. LeVeque. Clawpack: Building an open source ecosystem for solving hyperbolic PDEs. 2(68), August 8 2016.

[21] IK Nikolos and AI Delis. An unstructured node-centered finite volume scheme for shallow water flows with wet/dry fronts over complex topography. *Computer Methods in Applied Mechanics and Engineering*, 198(47-48):3723–3750, 2009.

[22] Carlos Sánchez-Linares, Marc de la Asunción, Manuel J Castro, José M González-Vida, Jorge Macías, and Siddhartha Mishra. Uncertainty quantification in tsunami modeling using multi-level monte carlo finite volume method. *Journal of Mathematics in Industry*, 6(1):1–26, 2016.

[23] Lixiang Song, Jianzhong Zhou, Qingqing Li, Xiaoling Yang, and Yongchuan Zhang. An unstructured finite volume model for dam-break floods with wet/dry fronts over complex topography. *International Journal for Numerical Methods in Fluids*, 67(8):960–980, 2011.

[24] Eleuterio F Toro. *Shock-capturing methods for free-surface shallow flows*. Wiley-Blackwell, 2001.